ADVANCED MATERIALS
www.advmat.de

A Disordered Rock Salt Anode for Long-Lived All-Vanadium Sodium-Ion Battery

Haichen Lin, Zishen Wang, Oliver Solares, Steven Huber, Jan Hofmann, Simon Danitz, Wei-Tao Peng, Ke Zhou, Ping-Che Lee, Haodong Liu, Zeyu Hui, Runze Liu, Mengchen Liu, Wei Tang, Junlin Wu, Zheng Chen, Karena W. Chapman, Shyue Ping Ong,* and Ping Liu**

Rechargeable batteries wherein both the cathode and the anode are vanadium-based phases are promising grid-energy storage candidates, offering long cycle life and easy recycling. However, their system-level energy density must be improved to lower their footprint and operating costs. In this work, an all-vanadium sodium-ion battery that uses a new disordered rock salt (DRS) anode, $Na_3V_2O_5$ (DRS-NVO), is proposed. For DRS-NVO, ≈2 Na^+ ions can be reversibly cycled at ≈0.7 V versus Na/Na^+. Structural characterization by X-ray diffraction and pair distribution function (PDF) analysis reveal increased local distortions during Na^+ insertion but the overall DRS structure is maintained. The material shows exceptional stability and rate capability, achieving 10 000 cycles in half-cell tests at rates of up to 20 C. Molecular dynamics simulations produce voltage profiles and ion diffusivities in good agreement with experimental results. Pairing the DRS-NVO anode with a $Na_3V_2(PO_4)_3$ (NVP) cathode yields a cell (NVO|NVP) voltage of 2.7 V, with symmetric voltage profiles and an energy efficiency >93%. This all-vanadium sodium-ion battery exhibits excellent cycling stability, retaining 80% of its capacity after 3 000 cycles. Levelized cost-of-storage (LCOS) evaluations based on a cell design model confirm the cost-effectiveness, positioning NVO|NVP as a competitive grid-scale energy storage solution.

1. Introduction

Energy storage systems designed for the electric grid need to work at diverse time scales and durations, from short-term grid stability (seconds to minutes) to long-duration renewable energy integration (hours to days).[1,2] A wide variety of cell chemistries has been explored to address these different needs.[3,4] Despite the dominance of lithium-ion batteries, the need for long service life (>30 years) and concerns for supply chain and resource accessibility have led to the consideration of several aqueous batteries, flow batteries, and sodium-ion batteries.[5–8] Vanadium is a versatile redox-active transition metal with promising applications in energy storage.[9] Vanadium is more abundant in the Earth's crust than nickel (Ni), copper (Cu), and zinc (Zn), and its broad range of oxidation states, from +5 to 0, makes it suitable for energy storage devices that operate with redox reactions involving the same metal element in both the anode and the cathode.[10–13] Currently, vanadium is primarily used as an additive in the steel industry.[14]

All-vanadium redox flow battery (VFB) is the best-known example of vanadium's use in energy storage.[15–18] This technology utilizes V redox couples (V^{3+}/V^{4+} and V^{2+}/V^{3+}) on both the cathode and the anode, yielding a theoretical voltage of 1.26 V. The practical energy density of VFB is ≈20 Wh kg^{-1}, largely limited by the solubility of the salts.[13] The large system footprint and the need to manage the large volume of electrolytes during operation translate into increased operating costs.[19]

H. Lin, Z. Wang, S. Huber, S. Danitz, H. Liu, Z. Hui, R. Liu, M. Liu, W. Tang, J. Wu, Z. Chen, S. P. Ong, P. Liu
Aiiso Yufeng Li Family Department of Nanoengineering
University of California San Diego
La Jolla, San Diego, CA 92093, USA
E-mail: ongsp@ucsd.edu; piliu@ucsd.edu

H. Lin, Z. Wang, S. Huber, S. Danitz, W.-T. Peng, K. Zhou, H. Liu, Z. Hui, R. Liu, M. Liu, W. Tang, J. Wu, Z. Chen, S. P. Ong, P. Liu
Sustainable Power and Energy Center
University of California San Diego
La Jolla, San Diego, CA 92093, USA

The ORCID identification number(s) for the author(s) of this article can be found under https://doi.org/10.1002/adma.202503143

DOI: 10.1002/adma.202503143

Z. Wang, R. Liu, S. P. Ong
Energy Storage Research Alliance
Argonne National Laboratory
9700 South Cass Avenue, Lemont, IL 60439, USA

O. Solares, J. Hofmann, K. W. Chapman
Department of Chemistry
Stony Brook University
100 Nicolls Rd, Stony Brook, NY 11794, USA
E-mail: karena.chapman@stonybrook.edu

P.-C. Lee, P. Liu
Material Science and Engineering program
University of California San Diego
La Jolla, San Diego, CA 92093, USA

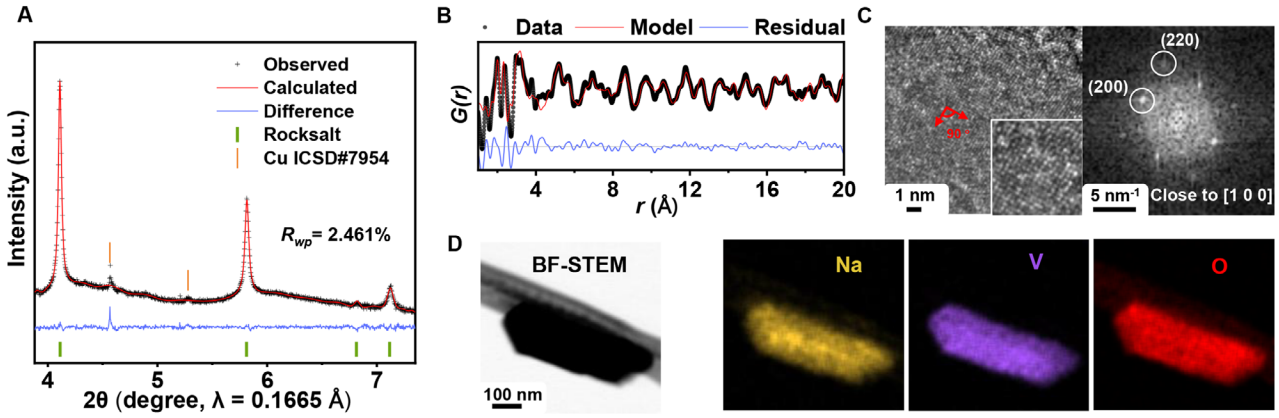

Figure 1. Structural and compositional characterization of DRS-NVO. A) Le Bail refinement of synchrotron PXRD for DRS-NVO. B) PDF data fit with a two-phase model composed of a crystalline DRS and a distorted DRS structure. C) HRTEM images and FFT analysis of DRS-NVO showing a rock-salt structure. D) STEM-EDS elemental mapping showing uniform Na, V, and O distribution within the DRS-NVO particle.

In the past few years, searches for vanadium-based energy storage solutions have focused on developing systems that offer increased cell voltage and higher energy and power densities than VFBs.[20] One promising option is the all-vanadium sodium-ion battery, leveraging the abundance and low cost of Na.[21] A notable example is the $Na_3V_2(PO_4)_3$ (NVP, a NASICON material) symmetric sodium-ion battery, which uses NVP as both the anode (V^{2+}/V^{3+} at 1.6 V vs Na/Na^+) and the cathode (V^{3+}/V^{4+} at 3.3 V vs Na/Na^+).[22–26] This configuration has demonstrated good cycling stability and rate capability. The elevated potential of the NVP anode, as compared to the commonly used hard carbon with a plateau at <0.1 V, is also expected to mitigate the risk of Na metal plating during fast charging events, thus improving safety.[27,28] While NVP exhibits high stability as an anode, its high working potential results in a low cell voltage and much-reduced energy density. This limitation is similar to that of $Li_4Ti_5O_{12}$ (LTO) as an anode in lithium-ion batteries, which is also highly stable and offers good rate capability but suffers from a high potential (≈1.5 V vs Li metal).[29] Consequently, the working potential of NVP|NVP is ≈1.7 V, which is relatively modest for a nonaqueous electrolyte system.

In 2020, we reported a disordered rock salt (DRS) anode for Li-ion batteries, DRS-$Li_3V_2O_5$ (DRS-LVO).[30] DRS-LVO can be cycled reversibly with ≈2 Li intercalating/extracting at an average potential of 0.6 V, significantly lower than other oxides.[29,31,32] It also exhibits excellent rate capability and long cycle life. We have thus been intrigued by two questions: 1) Can a sodium analog of the DRS structure be formed by intercalating Na^+ into V_2O_5? 2) Would this sodium-based material share the same working mechanism and properties as DRS-LVO since Na^+ (1.02 Å) is much bigger than Li^+ (0.76 Å)?

Here, we report the in situ formation of DRS-$Na_3V_2O_5$ (DRS-NVO) during electrochemical Na^+ insertion. The material can reversibly accommodate ≈2 additional Na^+ at an average voltage of ≈0.7 V. By combining theoretical calculations and X-ray total scattering experiments, we found that DRS-NVO undergoes a reversible structural transformation involving the formation of structurally distorted local domains which offers a contrast to DRS-LVO for which the DRS is retained throughout. This results in a voltage-capacity profile that is substantially linear without any discernable plateaus. DRS-NVO is capable of cycling 10 000 cycles at rates of up to 20 C in half-cell tests with minor capacity loss. Pairing it with NVP yields an all-vanadium sodium-ion battery, NVO|NVP, with an operating voltage of 2.7 V, a projected energy density of 103 Wh kg^{-1}, along with stability for 3000 cycles, and an energy efficiency of over 93%. These attributes make NVO|NVP a promising candidate for grid-storage applications.

2. Formation and Structure of DRS-NVO

DRS-NVO is synthesized via an in situ electrochemical method by directly discharging V_2O_5 to 0.01 V, during which ≈5 Na^+ ions are intercalated, followed by charging up to 1.4 V, removing ≈2 Na^+ ions, as shown in Figure S1 (Supporting Information). We observed the formation of a disordered rock salt structure ($Fm\bar{3}m$, a = 4.642(1) Å). The cubic lattice dimension was determined by Le Bail refinement of synchrotron PXRD data (**Figure 1A**). Interestingly, if V_2O_5 is intercalated with only 3 Na^+, without further intercalation up to 5 Na^+ and subsequent charging, a mixed-phase state is observed, consisting of both layered and rock salt structures (Figure S2, Supporting Information). This behavior contrasts with the Li version (DRS-LVO), where V_2O_5 directly transforms into the ω-phase (rock salt phase) upon the insertion of ≈3 Li^+ ions.[30,33]

The crystalline DRS model effectively describes the long-range features of the PDF data, however residual peaks at r < 5 Å suggest the presence of local structural distortions that deviate from this average model (Figure S3, Supporting Information). To model these local distortions, we constructed a DRS supercell ($Na_{25}V_{16}O_{40}$, denoted DRS-Na3125) and relaxed this structure using DFT calculations (Figure S4, Supporting Information), which minimizes the total energy and allows atoms to deviate from their high symmetry positions. The radial distribution function (RDF) of the DRS-Na3125 model was calculated to help interpret the experimental data (Figure S5, Supporting Information). In the low-r region, peaks at ≈2.0, ≈2.3, ≈3.0 and ≈3.2 Å correspond to V—O, Na—O, O—O and V/Na-V/Na interatomic distances. Ultimately, the best fit to the experimental PDF (R_{WP} = 0.47) was obtained with a 2-phase model comprising the regular DRS structure and the locally distorted "DRS-Na3125" phase (Figure 1B).

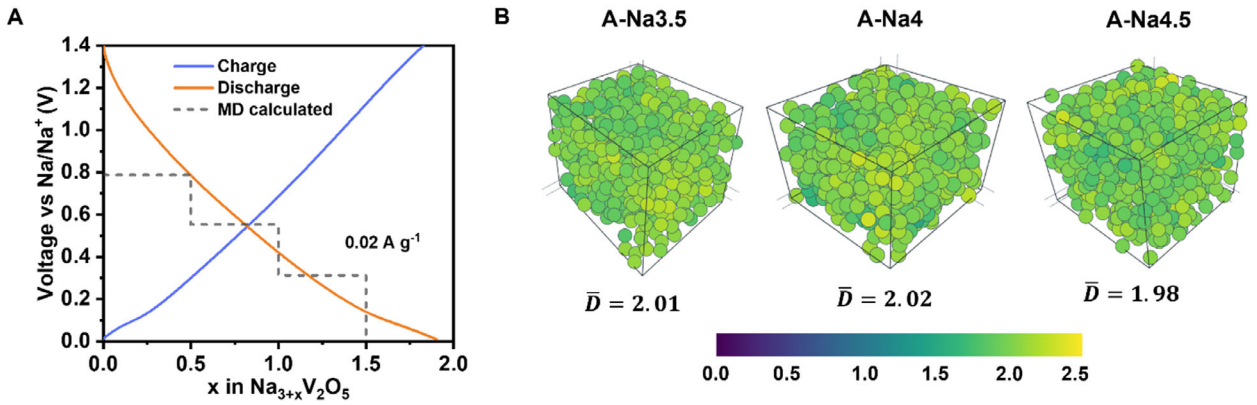

Figure 2. Thermodynamics of the DRS-NVO electrode reaction. A) Voltage profile of DRS-NVO cycled at a low rate (0.02 A g^{-1}) to approximate thermodynamic equilibrium. The calculated voltage at 3 different x values is included for comparison. B) Supercell models with highly distorted structural features at different Na contents. The Steinhardt's order parameter, $\bar{D}$ values are shown below. Higher values indicate a greater degree of disorder.

This suggests that while DRS-NVO retains an overall rock salt framework, localized distorted regions emerge to accommodate additional Na^+.

High-Resolution Transmission Electron Microscopy (HRTEM) provides detailed insights into the local structure of DRS-NVO. As shown in Figure 1C, DRS-NVO exhibits consistent crystallinity in the local regions, with fast Fourier transform (FFT) results showing clear (200) and (220) peaks, consistent with the cubic rock salt structure. The atomic distance distribution along the [1 0 0] direction (Figure S6, Supporting Information) shows a *d*-spacing of ≈4.6 Å, which is consistent with the result from powder diffraction analysis.

The morphology of the DRS-NVO particles, characterized by Field Emission Scanning Electron Microscopy (FESEM), is shown in Figure S7 (Supporting Information). This reveals a primary particle size of ≈1 µm. Elemental mapping of a single DRS-NVO particle, presented in Figure 1D, was performed using STEM-EDS (Scanning Transmission Electron Microscopy – Energy Dispersive X-ray Spectroscopy), which confirmed the uniform distribution of Na, V, and O throughout the particle. The Na/V ratio of DRS-NVO was further confirmed through inductively coupled plasma optical emission spectrometry (ICP-OES, bulk analysis, Figure S8, Supporting Information) and compared with values obtained from analysis by FESEM-EDS (localized analysis, Figure S9, Supporting Information) and STEM-EDS (single-particle analysis, Figure S10, Supporting Information).[34] The results, summarized in Table S1 (Supporting Information), indicate a nominal composition of $Na_3V_2O_5$.

3. Thermodynamics of the DRS-NVO Electrode Reaction

To demonstrate the application of DRS-NVO as an anode for Na-ion batteries, we investigated the thermodynamics of Na^+ insertion. The in situ formed DRS-NVO was fully discharged to 0.01 V and cycled between 0.01 and 1.4 V at a low current of 0.02 A g^{-1} to approximate a thermodynamic equilibrium (**Figure 2A**). Approximately 2 Na^+ ions were reversibly inserted and extracted during the cycle. Elemental characterization (Figures S8–S10, Supporting Information) results of fully discharged DRS-NVO at 0.01 V are summarized in Table S1 (Supporting Information) and compared with DRS-NVO, confirming a ~2 Na^+ difference before and after full discharge, consistent with the discharge capacity observed in the voltage profile.

Interestingly, the voltage-composition profile is substantially linear with an average potential of ≈0.7 V and no noticeable hysteresis. This contrasts with the case of DRS-LVO, which features a distinct plateau at ≈0.6 V versus Li. A comparison of their voltage and dQ/dV profiles is provided in Figure S11 (Supporting Information). This difference suggests a distinct cation storage mechanism in DRS-NVO compared to DRS-LVO.[30] At first glance, this sloping voltage profile might suggest pseudo-capacitive behavior, similar to that observed in high surface area anode materials for sodium-ion batteries.[35,36] However, the large reversible capacity and modest surface area prompted us to consider bulk insertion-storage mechanisms.

One hypothesis is the formation of distorted regions within the DRS structure. The larger ionic radius of Na^+ compared to Li makes it less favorable for the inserted Na^+ ions to occupy tetrahedral interstices within the DRS lattice,[37,38] as occurs for Li^+ ions in DRS-LVO.[30] The formation of highly distorted (or near amorphous) local domains with lower symmetry offers a plausible mechanism for accommodating additional Na^+.[39]

DFT calculations provide insights into this structural distortion that occurs at high Na loadings. Following a similar approach to DRS-LVO,[40] we introduced excess Na into the structure by populating tetrahedral sites to construct a Na-rich model of $Na_nV_2O_5$ where n is 3.5, 4, or 4.5. Figure S12 (Supporting Information) illustrates the structural evolution before and after DFT relaxation, confirming distortion at the tetrahedral sites, which leads to the formation of locally distorted regions. Figure S13 (Supporting Information) shows the result of the representative DFT-relaxed DRS-Na4 structure, which reveals distorted features in Na-rich regions, contrasting with V-rich regions, which retain some regular DRS local structure. These findings highlight the divergent structural characteristics of Na- and Li-based DRS systems at extreme Li^+/Na^+ loadings.

To further evaluate the structural distortion in the DRS, we performed molecular dynamics (MD) simulations using a universal machine learning interatomic potential (uMLIP, see Methods)

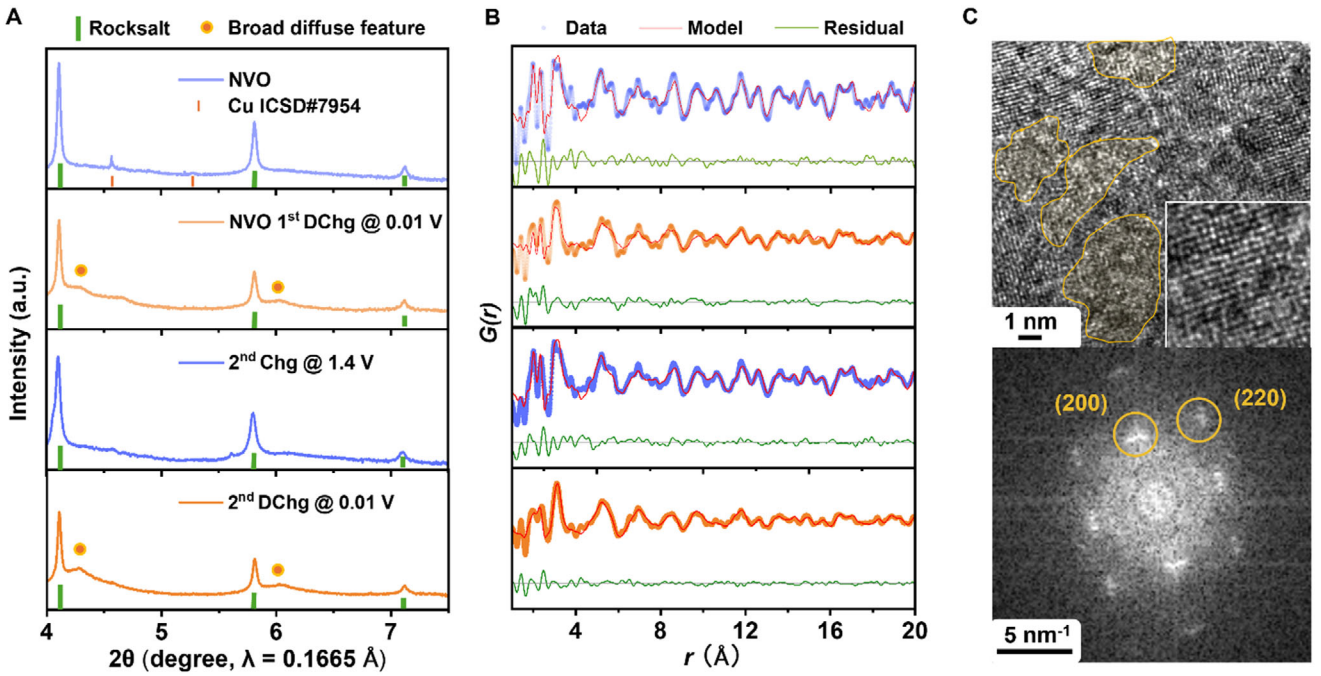

Figure 3. Reversible structural transformation of DRS-NVO during cycling. A) ex situ synchrotron PXRD patterns of DRS-NVO at 1.4 and 0.01 V during sequential cycling at a consistent low current of 0.02 A g^{-1}. Residual peaks at ≈4.6° and ≈5.3° originate from Cu powder introduced during the electrode-scratching process. B) PDFs at different voltages fitted with the two-phase composite model. A typical Rwp value is 0.47 as in the case of the fit for NVO. C) HRTEM images and FFT analysis of DRS-NVO at a fully discharged state (0.01 V vs Na). The distorted region in the fully discharged state is highlighted.

trained using a highly accurate MatPES dataset and an equivariant TensorNet architecture.[41,42] A melt-quench-anneal process is applied onto a ≈700-atom supercell of the DFT-relaxed DRS structure at three Na contents: $Na_{3.5}V_2O_5$ (A-Na3.5), $Na_4V_2O_5$ (A-Na4), and $Na_{4.5}V_2O_5$ (A-Na4.5). Figure 2B illustrates those three supercell models, each ball in the supercell model representing an individual atom (Na, V, or O atom) in the structure, with the color intensity (dark to light) indicating the degree of local distortion. The averaged Steinhardt's order parameter $\bar{D}$[43] of ≈2 for A-Na3.5, A-Na4, and A-Na4.5 are comparable with the previous report, suggesting the highly distorted state.[44] The approximate voltage profile computed from the highly distorted sodiated structures (Figure 2A) using the TensorNet uMLIP is also in good agreement with the experimental voltage profile. This structural distortion behavior is further corroborated by direct chemical sodiation using Sodium Naphthalenide (Naph-Na).[43] V_2O_5 was reacted with Naph-Na at two different mole ratios, 1:3 and 1:3.5. As shown in Figure S14 (Supporting Information), XRD patterns confirmed the formation of a rock-salt structure at a ratio of 1:3. In contrast, for the material synthesized at a ratio of 1:3.5, no distinct peaks were observed across the spectrum, indicating the presence of highly distorted structure in the as-synthesized material. Chemically formed DRS-NVO is thus similar to that formed by electrochemical sodiation.

4. Structural Analysis of DRS-NVO During Cycling

To examine the structural changes after cycling, a series of synchrotron total scattering measurements were carried out on the anode material recovered following consecutive cycles. As shown in Figure S15 (Supporting Information), in situ formed DRS-NVO was cycled at a low rate of 0.02 A g^{-1}, discharged to 0.01 V, charged back to 1.4 V, and then re-discharged to 0.01 V, with ex situ data collected at these four points. The discharge voltage curves had near identical shape, reflecting the reversibility of the process.

As shown in **Figure 3**A, when DRS-NVO was first discharged to 0.01 V, a series of broad diffuse features were observed at higher angles (i.e., smaller *d*-spacings) near the high-intensity DRS-NVO XRD peaks (200, 220) at 4.3° and 6.0°, suggesting the formation of a highly distorted structural component. Upon subsequent charging to 1.4 V, these broad diffuse features disappear, indicating a reversible restoration of the ordered state. These changes were repeated in the following cycles, demonstrating the reversible nature of the structure transition during cycling.

As shown in Figure 3B, PDFs of the recovered electrode were effectively fit using a two-phase model. The retention of long-range structural features after the insertion and extraction of two additional Na^+ ions suggests that the average rock salt structure remains intact throughout cycling. However, significant changes in the short-range structure are evident. Differential PDFs, which isolate structural changes following Na^+ insertion/extraction (Figure S16, Supporting Information), were well-modeled by the DRS-Na3125 model, where atomic positions deviate from the average long-range positions. This indicates the formation and elimination of distorted domains within the rock salt lattice during cycling.

HRTEM again provides additional insights into the local structure of DRS-NVO at the full discharge state (0.01 V). In Figure 3C, we can see that while some local regions retain the rock salt

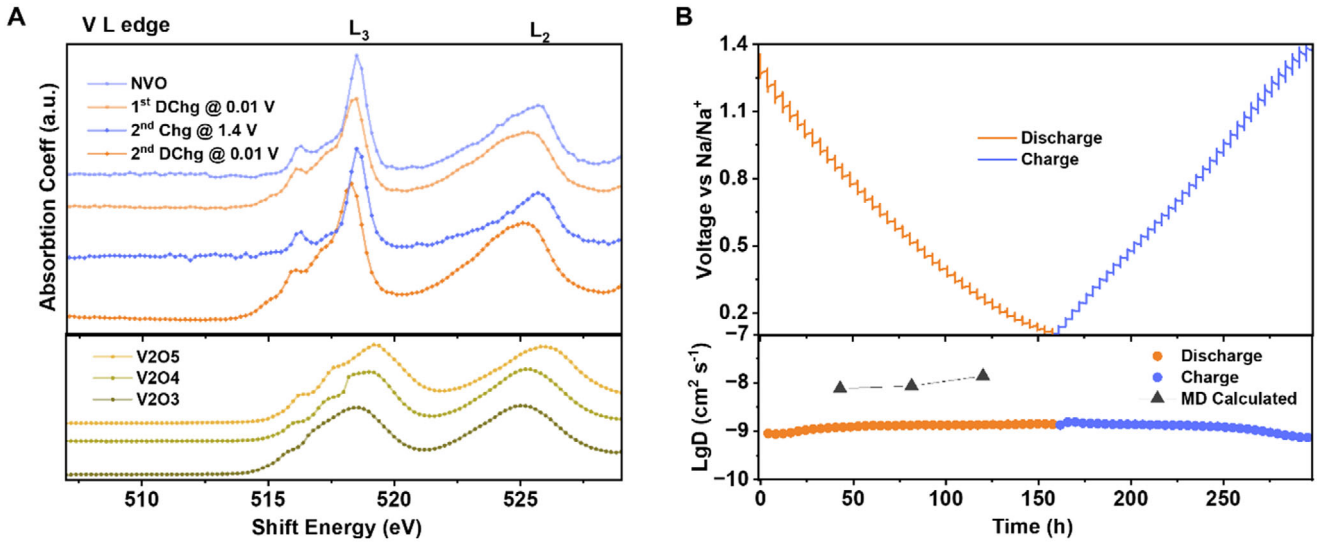

Figure 4. Charge compensation mechanism and kinetics of DRS-NVO. A) Experimental V L-edge XANES spectra at different states of (dis)charge, with V oxides of varying oxidation states measured as references. B) Voltage profile from GITT measurement and comparison of D_{eff} values obtained from GITT and MD.

structure, distorted regions are distributed among these crystalline areas. This observation is consistent with the diffuse features observed in the synchrotron PXRD patterns. Additionally, FESEM images of fully discharged DRS-NVO within the electrode (Figure S17, Supporting Information) show no significant morphological changes compared to the DRS-NVO powder, confirming the structural stability of the material during cycling. Cross-sectional images of DRS-NVO and discharged DRS-NVO are compared in Figure S18 (Supporting Information), with no obvious thickness differences. Furthermore, the PXRD patterns of the material after 50, 100, and 500 cycles at 5C (Figure S19, Supporting Information) confirm that the DRS peaks remain stable. The diffusion features near the main peaks become broader and shift slightly toward higher angles, which may be attributed to the growing local distortion and formation of local domains with shorter bonding distances (e.g., V–O ≈2.0 Å), leading to smaller d-spacing.

5. Charge Compensation and Reaction Kinetics of DRS-NVO

The charge compensation mechanism of DRS-NVO was examined using normalized V L-edge X-ray absorption near-edge structure (XANES) spectra (**Figure 4A**). The V L_3 and L_2 edges appear as two characteristic peaks in the spectra, located at 517–520 eV and 524–526 eV, respectively. The spectra reveal that V undergoes a reversible redox process during cycling, as evidenced by reversible peak shifts and shape changes. To compare the valence states of V at different charge states in DRS-NVO, standard reference powders of V_2O_5 (V^{5+}), V_2O_4 (V^{4+}), and V_2O_3 (V^{3+}) were used. The valency of V in DRS-NVO at different charge states is derived from the V L_3 peaks. As shown in Figure S20 (Supporting Information), V undergoes a reversible redox process during cycling. Finally, for the V L_2 edge, a broader peak is observed in the discharged materials, indicating a more complex local environment due to the increased Na content.

The kinetics of DRS-NVO were evaluated using the Galvanostatic Intermittent Titration Technique (GITT). As shown in Figure 4B, both charge and discharge voltage profiles exhibit a single slope, consistent with previous thermodynamics observations. Diffusion coefficients (D_{eff}) show only slight variations throughout the cycle, on the order of 10^{-9} cm^2 s^{-1}. These findings are further corroborated by the D_{eff} values in the A-Na3.5, A-Na4, and A-Na4.5 structures obtained from MD simulations with the uMLIP (see details in Method Section, Supporting Information). The experimental and computational results are in the same order of magnitude. Additionally, both GITT and MD calculations reveal that higher Na content contributes to slightly higher D_{eff}. This trend can be explained by the highly disordered nature of the material, where an increased number of activated cations enhances the formation of more effective percolation channels.[44] These findings confirm the favorable kinetics of DRS-NVO, and its related rate performance will be further discussed in the subsequent half-cell tests.

6. Electrochemical Performance of DRS-NVO

The electrochemical performance of DRS-NVO was first evaluated in a half-cell configuration using a Na metal foil as the counter electrode. **Figure 5A** presents the cycling stability under various rates (5 C, 10 C, and 20 C). The C rate is defined assuming a capacity of 200 mAh g^{-1} between 0.01 and 1.4 V. Corresponding voltage profiles are shown in Figure 5B. DRS-NVO demonstrated remarkable stability, maintaining ≈80% capacity after 10 000 cycles. Voltage profiles at different rates for the 1000th, 5000th, and 10 000th cycles, shown in Figure S21 (Supporting Information), feature consistent shapes. This remarkably stable electrochemical performance is likely related to the robust rock salt framework and the reversible localized structural distortion. Additionally, coin cells cycled for 10 000 cycles were disassembled to examine internal changes. The optical images are shown in Figure S22 (Supporting Information). The electrodes

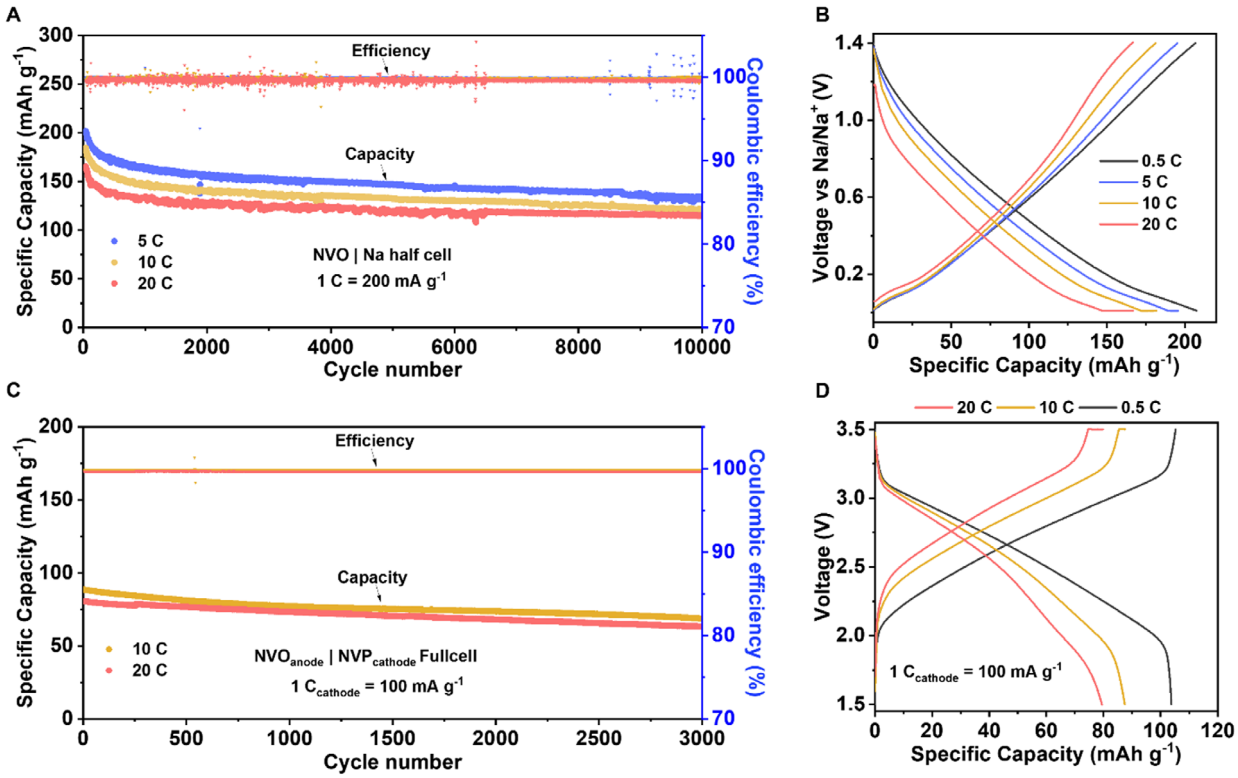

Figure 5. Electrochemical performance of DRS-NVO. A) Cycling stability of half-cells at various charge–discharge rates (5 C, 10 C, and 20 C, with 1 C = 200 mA g^{-1}) within a voltage window of 0.01–1.4 V. B) Voltage profiles of half-cells under different rates. C) Cycling stability of all-vanadium Na-ion battery (NVO|NVP) at 10 C and 20 C where 1 $C_{cathode}$ = 100 mA g^{-1}. D) Voltage profiles of the full cell at 0.5 C, 10 C, and 20 C within a voltage window of 1.5–3.5 V.

remained intact after cycling, and the unchanged color of the separator suggests no dissolution of vanadium species occurred during the prolonged cycling. Note that expanding the cycling voltage range to 0.01–2 V yields a capacity of over 300 mAh g^{-1} by removing more sodium on charging, however, the cycling stability is compromised likely related to a loss of the DRS structure which is favors a Na to V ratio of >3:2 (Figure S23, Supporting Information).

To demonstrate an all-vanadium sodium-ion battery, NVP was selected as the cathode to pair with DRS-NVO. The negative-to-positive electrode capacity ratio was set at 1.05:1, with the capacity calculated based on the cathode loading. The representative voltage profile, shown in Figure S24 (Supporting Information), reflects the combined contributions of the anode and cathode and demonstrates a cell working potential of 2.7 V. The cycling stability of NVO|NVP full cells under elevated rates (10C and 20C) is shown in Figure 5C. Here, the C rate is defined based on the nominal capacity of the cathode (100 mAh g^{-1}). Full cells operated at both rates maintained a capacity of over 80% after 3000 cycles. We note that our NVP electrode was not optimized (Figures S25 and S26, Supporting Information). Further improvement is expected to fully realize the intrinsic stability of NVO to exceed 10 000 cycles. Voltage profiles at different rates, shown in Figure 5D, are highly symmetric, demonstrating an energy efficiency of over 93% at 0.5 C and 90% at 10 C. The first-cycle coulombic efficiency exceeds 90% (Figure S27, Supporting Information). A comparison between two all-vanadium sodium-ion batteries, NVO|NVP and NVP|NVP, is presented in the Ragone plots (Figure S28, Supporting Information). For a fair evaluation, all the specific power and energy values are calculated based on the active material weight only. NVO|NVP demonstrates a clear advantage in specific energy, largely due to its higher working potential (2.7 V) compared to NVP|NVP (1.7 V).

To evaluate the potential of NVO|NVP as a candidate for grid energy storage, we performed a cell design exercise for NVO|NVP and NVO|NVP (Table S2, Supporting Information). Assuming an areal capacity of 3 mAh cm^{-2}, the respective projected energy densities based on the weight of the active stack (not including tabs and packaging) were 103 Wh kg^{-1} for NVO|NVP and 54 Wh kg^{-1} for NVP|NVP. Based on this projected cell performance data, we further estimated the LCOS and compared it with VFBs. The LCOS (dollars per kWh per cycle) here, was calculated assuming a vanadium price of \$25 kg^{-1},[45] and 10000 charge–discharge cycles. As shown in Table S3 (Supporting Information), the LCOS values for VFB, NVP|NVP, and NVO|NVP were 0.125, 0.045, and 0.024, respectively. These results emphasize the potential of NVO|NVP as a cost-effective solution for grid storage.

7. Conclusion

In summary, we have discovered a disordered rock salt anode material, DRS-NVO, for Na-ion batteries. The material is formed in situ by electrochemically inserting Na^+ down to a potential

of near 0 V versus Na and charging it to a potential of 1.4 V. The material exhibits a distinct mechanism compared to its Li-ion counterpart, DRS-LVO, to accommodate the larger Na^+. Rather than intercalating Na^+ into tetrahedral sites, DRS-NVO forms additional highly distorted domains while retaining the overall DRS structure. This process results in a substantially linear voltage profile. Approximately 2 Na^+ can reversibly intercalate and extract, yielding an average potential of ≈0.7 V. Both the working potential and the reversible structural transformation process are corroborated with DFT and MD simulation results. In kinetic studies, both GITT measurements and MD simulations show the Na^+ diffusion coefficient is largely independent of Na^+ concentration in the structure, highlighting exceptional Na^+ transport properties. DRS-NVO demonstrated remarkable long-term cycling stability, maintaining performance for up to 10000 cycles at 5 C, 10 C, and 20 C. DRS-NVO is paired with NVP to form an all-vanadium sodium-ion battery (NVO|NVP). The battery operates at a working potential of 2.7 V with a highly symmetric profile, stability of over 3000 cycles at elevated rates (10 C and 20 C), and high energy efficiency (≈93%). Furthermore, a cell design study shows NVO|NVP with a projected energy density of about 2x of NVP|NVP and estimated LCOS is 5x lower than VFBs. The performance metrics of DRS-NVO also position it as a promising complement to common anode materials (e.g., hard carbon, alloy) for high-power and long-life applications (Figure S29, Supporting Information).

Future research will focus on more in-depth structural characterization using advanced in situ techniques. In addition, efforts will aim to improve electrode and cell engineering for optimizing overall cell performance. We hope this work inspires continued exploration of disordered rock salt materials as stable and robust anodes for sodium-ion batteries.

Supporting Information

Supporting Information is available from the Wiley Online Library or from the author.

Acknowledgements

H.L., Z.W., and O.S. contributed equally to this work. This work was partially supported as part of GENESIS: A Next Generation Synthesis Center, an Energy Frontier Research Center funded by the U.S. Department of Energy, Office of Science, Basic Energy Sciences under Award Number DE-SC0019212 to P.L and K.C. This work was partially supported by the Office of Vehicle Technologies of the U.S. Department of Energy through the Advanced Battery Materials Research (BMR) Program (LENS Consortium) to P. L. through Argonne National Laboratory. The computational work (Z. Wang and S. P. Ong) is supported by the Energy Storage Research Alliance "ESRA" (DE-AC02-06CH11357), an Energy Innovation Hub funded by the U.S. Department of Energy, Office of Science, Basic Energy Sciences. The computational portions of this work used the National Energy Research Scientific Computing Center (NERSC) and Expanse at the San Diego Supercomputer Center. This work was performed in part at the San Diego Nanotechnology Infrastructure (SDNI) of UCSD, a member of the National Nanotechnology Coordinated Infrastructure (NNCI), which is supported by the National Science Foundation (Grant ECCS-1542148). This research used resources at the 28-ID-1 beamline of the National Synchrotron Light Source II, a the US DOE Office of Science User Facility operated for the DOE Office of Science by the Brookhaven National Laboratory under contract No. DE-SC0012704. The work at the ALS Beamline 8.0.1 was supported by DOE EERE VTO under the Applied Battery Materials Program, both under contract No. DE-AC02-05CH11231.

Conflict of Interest

A patent disclosure is filed with the University of California San Diego's Office of Innovation and Commercialization.

Data Availability Statement

The data that support the findings of this study are available from the corresponding author upon reasonable request.

Keywords

all vanadium, disordered rock salt, long-life, pair distribution function, sodium-ion

Received: February 15, 2025
Revised: May 20, 2025
Published online:

[1] J. Liu, J. Xiao, J. Yang, W. Wang, Y. Shao, P. Liu, M. S. Whittingham, *Next Energy* **2023**, *1*, 100015.
[2] M. R. Palacín, A. de Guibert, *Science* **2016**, *351*, 1253292.
[3] M. Shahjalal, P. K. Roy, T. Shams, A. Fly, J. I. Chowdhury, M. R. Ahmed, K. Liu, *Energy* **2022**, *241*, 122881.
[4] S. Windisch-Kern, E. Gerold, T. Nigl, A. Jandric, M. Altendorfer, B. Rutrecht, S. Scherhaufer, H. Raupenstrauch, R. Pomberger, H. Antrekowitsch, *Waste Manage.* **2022**, *138*, 125.
[5] X. Liu, Z. Wu, L. Xie, L. Sheng, J. Liu, L. Wang, K. Wu, X. He, *Energy Environ. Mater.* **2023**, *6*, 12501.
[6] F. Li, Z. Wei, A. Manthiram, Y. Feng, J. Ma, L. Mai, *J. Mater. Chem. A* **2019**, *7*, 9406.
[7] Y. Liang, Y. Yao, *Nat. Rev. Mater.* **2023**, *8*, 109.
[8] M. Park, J. Ryu, W. Wang, J. Cho, *Nat. Rev. Mater.* **2016**, *2*, 16080.
[9] X. Xu, F. Xiong, J. Meng, X. Wang, C. Niu, Q. An, L. Mai, *Adv. Funct. Mater.* **2020**, *30*, 1904398.
[10] M. Chen, Q. Liu, S. W. Wang, E. Wang, X. Guo, S. L. Chou, *Adv. Energy Mater.* **2019**, *9*, 1803609.
[11] D. Rehder, *Interrelations Between Essential Metal Ions and Human Diseases*, Springer, Berlin, Heidelberg **2013**, pp. 139-169.
[12] B. Mukherjee, B. Patra, S. Mahapatra, P. Banerjee, A. Tiwari, M. Chatterjee, *Toxicol. Lett.* **2004**, *150*, 135.
[13] Á. Cunha, J. Martins, N. Rodrigues, F. Brito, *Int. J. Energy Res.* **2015**, *39*, 889.
[14] R. Moskalyk, A. Alfantazi, *Miner. Eng.* **2003**, *16*, 793.
[15] G. Kear, A. A. Shah, F. C. Walsh, *Int. J. Energy Res.* **2012**, *36*, 1105.
[16] C. Ding, H. Zhang, X. Li, T. Liu, F. Xing, *J. Phys. Chem. Lett.* **2013**, *4*, 1281.
[17] A. Trovo, M. Rugna, N. Poli, M. Guarnieri, *Ceram. Int.* **2023**, *49*, 24487.
[18] A. Aluko, A. Knight, *IEEE Access* **2023**, *11*, 13773.
[19] Z. Huang, A. Mu, L. Wu, B. Yang, Y. Qian, J. Wang, *ACS Sustainable Chem. Eng.* **2022**, *10*, 7786.
[20] G. F. Frate, L. Ferrari, U. Desideri, *Renewable Energy* **2021**, *163*, 1754.
[21] X. Zhang, Z. Zhang, S. Xu, C. Xu, X. Rui, *Adv. Funct. Mater.* **2023**, *33*, 2306055.
[22] A. Das, S. Majumder, A. R. Chaudhuri, *J. Power Sources* **2020**, *461*, 228149.

[23] Y. Zhang, H. Zhao, Y. Du, *J. Mater. Chem. A* **2016**, *4*, 7155.
[24] S. Li, Y. Dong, L. Xu, X. Xu, L. He, L. Mai, *Adv. Mater.* **2014**, *26*, 3545.
[25] W. Wang, Q. Xu, H. Liu, Y. Wang, Y. Xia, *J. Mater. Chem. A* **2017**, *5*, 8440.
[26] E. Gu, J. Xu, Y. Du, X. Ge, X. Zhu, J. Bao, X. Zhou, *J. Alloys Compd.* **2019**, *788*, 240.
[27] Y. Qi, Y. Lu, F. Ding, Q. Zhang, H. Li, X. Huang, L. Chen, Y. S. Hu, *Angew. Chem., Int. Ed.* **2019**, *58*, 4361.
[28] X. Guo, Y. Xue, H. Zhou, Y. Weng, J. Zhou, *ACS Appl. Mater. Interfaces* **2019**, *12*, 2407.
[29] M. Odziomek, F. Chaput, A. Rutkowska, K. Świerczek, D. Olszewska, M. Sitarz, F. Lerouge, S. Parola, *Nat. Commun.* **2017**, *8*, 15636.
[30] H. Liu, Z. Zhu, Q. Yan, S. Yu, X. He, Y. Chen, R. Zhang, L. Ma, T. Liu, M. Li, *Nature* **2020**, *585*, 63.
[31] L. Shen, S. Chen, J. Maier, Y. Yu, *Adv. Mater.* **2017**, *29*, 1701571.
[32] R. Inada, T. Mori, R. Kumasaka, R. Ito, T. Tojo, Y. Sakurai, *Int. J. Appl. Ceram. Technol.* **2019**, *16*, 264.
[33] C. Delmas, H. Cognac-Auradou, J. Cocciantelli, M. Ménétrier, J. Doumerc, *Solid State Ionics* **1994**, *69*, 257.
[34] Y. Shirazi Moghadam, A. El Kharbachi, Y. Hu, K. Wang, S. Belin, M. Fichtner, *ACS Mater. Lett.* **2022**, *5*, 125.
[35] X. Li, T. Zhang, Z. Chen, H. Fan, P. Hu, C. Cai, L. Zhou, *Mater. Today Energy* **2024**, *44*, 101637.
[36] H. Zhao, J. Zhong, Y. Qi, K. Liang, J. Li, X. Huang, W. Chen, Y. Ren, *Chem. Eng. J.* **2023**, *465*, 143032.
[37] Y. Kera, *J. Solid State Chem.* **1984**, *51*, 205.
[38] B. Xiao, F. Omenya, D. Reed, X. Li, *Nanotechnology* **2021**, *32*, 422501.
[39] Q. Wei, X. Chang, D. Butts, R. DeBlock, K. Lan, J. Li, D. Chao, D.-L. Peng, B. Dunn, *Nat. Commun.* **2023**, *14*, 7.
[40] H. Lin, W.-T. Peng, Z. Wang, J. Hofmann, S. M. Vornholt, H. Liu, S. Wang, J. Holoubek, K. Zhou, Q. Miao, S. Huber, K. W. Chapman, S. P. Ong, P. Liu, *ACS Mater. Lett.* **2025**, 699.
[41] T. W. Ko, B. Deng, M. Nassar, L. Barroso-Luque, R. Liu, J. Qi, E. Liu, G. Ceder, S. Miret, S. P. Ong, arXiv **2025**, arXiv:2503.03837.
[42] A. D. Kaplan, R. Liu, J. Qi, T. W. Ko, B. Deng, J. Riebesell, G. Ceder, K. A. Persson, S. P. Ong, arXiv **2025**, arXiv:2503.04070.
[43] W. Li, M. Fukunishi, B. J. Morgan, O. J. Borkiewicz, K. W. Chapman, V. Pralong, A. Maignan, O. I. Lebedev, J. Ma, H. Groult, *Chem. Mater.* **2017**, *29*, 1836.
[44] E. Uchaker, Y. Zheng, S. Li, S. Candelaria, S. Hu, G. Cao, *J. Mater. Chem. A* **2014**, *2*, 18208.
[45] K. E. Rodby, R. L. Jaffe, E. A. Olivetti, F. R. Brushett, *J. Power Sources* **2023**, *560*, 232605.